

Dynamics in the spin-boson model by maximum entropy moment imaging

D. Bailey, M. Hurley, and H. K. McDowell

Citation: *The Journal of Chemical Physics* **109**, 8262 (1998); doi: 10.1063/1.477488

View online: <http://dx.doi.org/10.1063/1.477488>

View Table of Contents: <http://scitation.aip.org/content/aip/journal/jcp/109/19?ver=pdfcov>

Published by the AIP Publishing

Articles you may be interested in

[Geometric phases and quantum correlations dynamics in spin-boson model](#)

J. Appl. Phys. **115**, 044909 (2014); 10.1063/1.4863401

[Dynamics of the sub-Ohmic spin-boson model: A time-dependent variational study](#)

J. Chem. Phys. **138**, 084111 (2013); 10.1063/1.4792502

[Surface-hopping dynamics of a spin-boson system](#)

J. Chem. Phys. **116**, 2346 (2002); 10.1063/1.1433502

[Basis set approach to the quantum dissipative dynamics: Application of the multiconfiguration time-dependent Hartree method to the spin-boson problem](#)

J. Chem. Phys. **113**, 9948 (2000); 10.1063/1.1323746

[Efficient memory equation algorithm for reduced dynamics in spin-boson models](#)

J. Chem. Phys. **110**, 138 (1999); 10.1063/1.478130



Dynamics in the spin-boson model by maximum entropy moment imaging

D. Bailey, M. Hurley, and H. K. McDowell

Department of Chemistry and Biochemistry, The University of Texas at Arlington, Arlington, Texas 76019-0065

(Received 26 January 1998; accepted 12 August 1998)

The spin-spin time correlation function of the spin-boson model is studied using a maximum entropy imaging procedure founded on knowledge of early time derivatives or moments of the corresponding spectral density. The coherent-incoherent boundary is reproduced in agreement with the results of dynamical path-integral Monte Carlo and the procedure is shown to be stable numerically at both long time and low temperature. © 1998 American Institute of Physics. [S0021-9606(98)51643-1]

I. INTRODUCTION

Quantum dynamics in the form of tunneling and phase coherence is an important aspect of dynamics in condensed phase and many-body systems where thermal averaging is an essential component.^{1,2} Significant progress has been made from a computational perspective with respect to incorporating quantum effects, particularly with regard to time correlation functions (TCF). The most prominent class of methodologies center around the use of path-integrals.³⁻⁵ The path integral approach is a powerful tool both computationally and as an interpretive instrument. On the other hand the approach is difficult to implement at longer times.^{1,6}

Another approach to dynamics in condensed phase systems is the method of generalized Langevin equation theory.⁷⁻¹⁰ This approach is founded on a formal partitioning of a global system into a system and a bath. We have explored this approach in the context of quantum TCFs using molecular time scale generalized Langevin equation theory (MTGLE).⁹⁻²⁰ A critical element of MTGLE theory is the use of short-time derivatives to construct the formal theory. As a by-product of these studies, we have developed powerful tools for imaging spectral densities using their moments.^{16,21-23} In particular, given the TCF $C(t)$, which will typically be an even function of time, we define the short-time derivatives as

$$C^{(2n)} = \left[\frac{d^{2n}C(t)}{dt^{2n}} \right]_{t=0} \quad (1)$$

and the spectral density as

$$\rho(\omega) = \frac{2}{\pi} \int_0^\infty dt C(t) \cos \omega t \quad (2)$$

with the moments given by

$$\rho^{(n)} = \int_0^\infty d\omega \omega^{2n} \rho(\omega) \quad (3)$$

$$= (-1)^n C^{(2n)}, \quad (4)$$

that is, the time derivatives are directly related to the power moments of the spectral density. Using the moments $\rho^{(n)}$, we

have shown that images of $\rho(\omega)$ can be constructed by a variety of procedures.^{16,21-23} The TCF is obtained through the inverse Fourier transform as

$$C(t) = \int_{\omega_a}^{\omega_b} d\omega \rho(\omega) \cos \omega t. \quad (5)$$

In this paper we apply one of these approaches, the Pmaxent method,²³ to study an important nonlinear, many-body system, the spin-boson model.^{1,2,24-61}

The spin-boson model, a classic two-level tunneling system coupled to a bath of oscillators, is given by the Hamiltonian

$$H = -K\sigma_x + H_{\text{bath}} + \sum_j C_j x_j \sigma_z, \quad (6)$$

where

$$H_{\text{bath}} = \sum_j \left[\frac{p_j^2}{2m_j} + \frac{m_j \omega_j^2 x_j^2}{2} \right], \quad (7)$$

m_j and ω_j are the mass and frequency of the j th oscillator, $\sigma_i (i=x,y,z)$ are Pauli spin matrices, $2K$ is the tunnel splitting, and C_j is the strength of the coupling to the j th oscillator. The bath oscillators and coupling coefficients are defined through the spectral distribution

$$J(\omega) = \frac{\pi}{2} \sum_j \frac{C_j^2}{m_j \omega_j} \delta(\omega - \omega_j). \quad (8)$$

In the present work we set this distribution as the Ohmic-exponential case given by³²

$$J(\omega) = \eta \omega e^{-\omega/\omega_c}, \quad (9)$$

where ω_c is a characteristic cutoff frequency. The time correlation function of interest is given by

$$C(t) = \frac{1}{2} \langle \{ \sigma_z(t), \sigma_z(0) \} \rangle \quad (10)$$

with time derivatives given by

$$C^{(2n)} = (-1)^n \frac{1}{2} \left\langle \left\{ \frac{\sigma_z^{(2n)}(0)}{i^{2n}}, \sigma_z(0) \right\} \right\rangle \quad (11)$$

and the brackets $\{\cdot\cdot\}$ indicate an anticommutator. The factor i^{2n} is included to remove the imaginary i from subsequent equations of motion. In a related approach the function

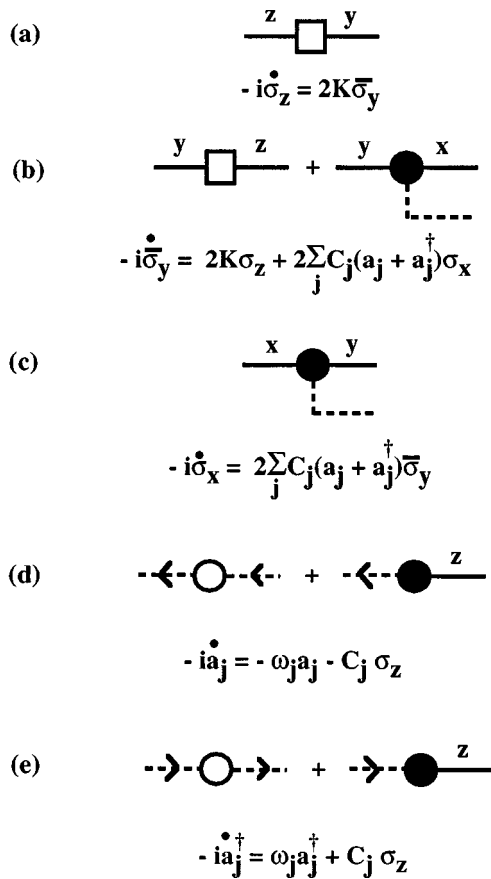


FIG. 1. Graphical representation of branching elements in equations of motion.

$\langle \sigma_z(t) \rangle$ has been studied where the brackets $\langle \cdots \rangle$ indicate an initial state having the spin in one of its two states and the bath thermally averaged with respect to the chosen spin state.³² We will not examine this function in the present work. In Appendix A we rewrite the Hamiltonian in Eq. (6) in a second-quantized form and scale using ω_c . We also review various required properties of the spin-boson model.

The spin-boson model has been the subject of considerable attention^{1,2,24–61} with a major review available.³² It has proven to be a major test case for dynamical path-integral Monte Carlo methods with the classic paper by Mak and Chandler as the first definitive numerical treatment of the model.³⁵ In this paper we will not focus on the spin-boson system per se but rather use it as a test system for examining the efficacy of the Pmaxent imaging process described in a companion paper.²³ In particular we are interested in obtaining the boundary between coherent and incoherent decay of the TCF, a manifestation of the loss of quantum coherence by dissipation from the bath of oscillators, and we compare our results with those of Mak and Chandler and with the noninteracting-blip approximation.^{27,32,60} We also examine stability of the TCF in Eq. (10) at long times using the Pmaxent approach and the direct use of the spectral density $\rho(\omega)$ to obtain decay times.

In Sec. II we describe a graphical process which facilitates computation of the time derivatives in Eq. (11). Section III is devoted to summarizing our imaging process for $\rho(\omega)$ which we call the Pmaxent process. In Sec. IV we obtain

results for $C(t)$ and compare with the results of Mak and Chandler.³⁵ We conclude in Sec. V with several summary remarks on the use of moment imaging methods to obtain time correlation functions.

II. GRAPHICAL DETERMINATION OF TIME DERIVATIVES

We have shown in previous work that the algebraic manipulations required to obtain the time derivatives or moments in Eq. (11) can be described efficiently by the use of a graphical process.²⁰ In particular the n th derivative of $\sigma_z(t)$ can be thought of as n graphical branch points, each branch point being due to a specific term in the equation of motion of a given operator. Thus, we begin by obtaining the following equations of motion using the Hamiltonian in Eq. (A4) and the Heisenberg equation of motion while defining $\bar{\sigma}_y(t) = i\sigma_y(t)$ to remove explicit dependence on $i = \sqrt{-1}$,

$$\frac{\dot{\sigma}_z(t)}{i} = 2K\bar{\sigma}_y(t), \quad (12)$$

$$\frac{\dot{\sigma}_y(t)}{i} = 2K\sigma_z(t) + 2\sum_j C_j(a_j(t) + a_j^\dagger(t))\sigma_x(t), \quad (13)$$

$$\frac{\dot{\sigma}_x(t)}{i} = 2\sum_j C_j(a_j(t) + a_j^\dagger(t))\bar{\sigma}_y(t), \quad (14)$$

$$\frac{\dot{a}_k(t)}{i} = -\omega_k a_k(t) - C_k\sigma_z(t), \quad (15)$$

and

$$\frac{\dot{a}_k^\dagger(t)}{i} = \omega_k a_k^\dagger(t) + C_k\sigma_z(t), \quad (16)$$

where the dot notation is used to indicate a time derivative. We explicitly pull out the factor i to avoid keeping up with it in our graphical analysis [see Eq. (11)]. As discussed in Appendix A, all quantities in this and the following sections are scaled by the cutoff frequency ω_c . Following our previous convention, we assume that the sequence of time derivatives in our graphs is taken in a left to right sense.²⁰ In Fig. 1 we present the basic graphical elements which match with the equations of motion in Eqs. (12)–(16). Solid lines with labels x , y , or z indicate the spin operators and dashed lines with labels indicate the bath operators $a_k(t)$ and $a_k^\dagger(t)$. To distinguish between $a_k(t)$ and $a_k^\dagger(t)$, we add a directional arrow which points to the left for $a_k(t)$ and to the right for $a_k^\dagger(t)$. We see in Fig. 1 that the element $2K$ is denoted by a box. The element ω_k is denoted by a circle on dashed lines. Note also that an additional minus sign must be carried for circles on the dashed line for $a_k(t)$. Nonlinear branch points are denoted by a solid circle and we describe these as nodes. Note that the node on $a_k(t)$ carries a minus sign.

We find in applying the graphical elements in Fig. 1 to obtain time derivatives that linear branch points appear in a characteristic pattern with respect to starting and ending at σ_z . We display the first few such composite linear elements in Fig. 2(a). We denote these composite elements by a circle on a σ_z -line with the symbol n_i inside the circle to indicate the number of derivatives in the composite element. This is

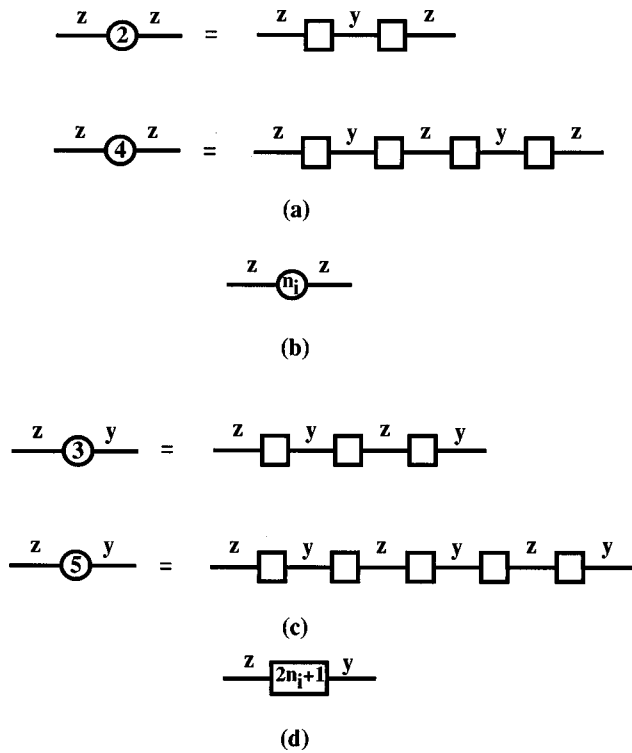


FIG. 2. Composite graphical elements for spin lines.

shown in Fig. 2(b). The number of derivatives must be an even number. Corresponding to this composite element, we find algebraically the contribution $(2K)^{n_i}$. Similarly, there is a characteristic pattern with respect to starting at σ_z and ending at σ_y or vice versa. This pattern is displayed in Fig. 2(c). We denote these composite elements by a box on a spin line with the symbol $2n_i+1$ inside the box to indicate the number of derivatives in the composite element. This is shown in Fig. 2(d). Corresponding to this composite element, we find algebraically the contribution $(2K)^{2n_i+1}$.

In Fig. 3 we display composite graphical elements for the linear branches which occur on the bath operators. In each case the symbol n_i has been added to the circle to indicate that n_i derivatives have been taken which produce the linear branch.

We turn next to examining the graphs used to determine the time derivatives. These graphs are classified according to the number of nonlinear branches or nodes that appear. We note from Eq. (11) that the only graphs which will contribute at time zero are those which contain the solid line for $\sigma_z(0)$ on the right-hand side with an even number of bath oscillators. Any other graph must give zero when anticommutated with $\sigma_z(0)$. As will become clear below, judicious use of

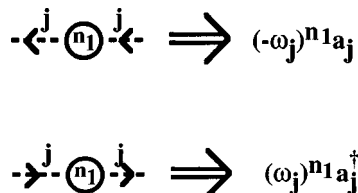


FIG. 3. Composite graphical elements for bath oscillator lines.

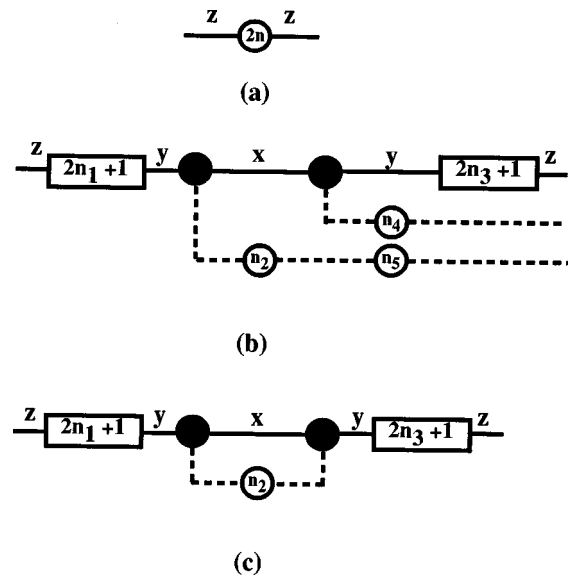


FIG. 4. Zero-node and two-node graphs.

Eqs. (A8) and (A10) greatly simplifies the algebraic task of computing derivatives.

The zero-node graph is given in Fig. 4(a). Algebraically, this graph corresponds to

$$\sigma_z^{(2n)}(0) = (2K)^{2n} \sigma_z(0) \quad (17)$$

which when substituted into Eqs. (4) and (11) yields

$$\rho^{(n)}(0) = (2K)^{2n}. \quad (18)$$

The zero in parentheses indicates zero node. The one-node graphs always produce a zero contribution.

The two-node graphs are given in Figs. 4(b) and 4(c). Note for simplicity that we do not assign arrows to the dashed lines in either graph. Assigning arrows is merely a matter of summing over $a_k(t)$ and $a_k^\dagger(t)$ and keeping up with the minus sign assigned to $a_k(t)$ as described above. Substitution of the algebraic analogue of the graph in Fig. 4(b) into Eqs. (4) and (11) yields

$$\begin{aligned} \rho^{(n)}(2) = & 4 \sum_{\{n\}} (2K)^{2n_1+2n_3+2} [2n_3+1, n_4, n_5] \\ & \times \sum_{jk} C_j C_k \omega_j^{n_2+n_5} \omega_k^{n_4} [(-1)^{n_2+n_5} a_j + a_j^\dagger] \\ & \times [(-1)^{n_4} a_k + a_k^\dagger], \end{aligned} \quad (19)$$

where

$$[n_1, n_2, \dots, n_p] = \frac{(\sum_{i=1}^p n_i)!}{\prod_{i=1}^p n_i!}, \quad (20)$$

and $\{n\}$ indicates a sum on all allowed integer values of n_1 to n_5 such that the constraint

$$2n = 4 + 2n_1 + n_2 + 2n_3 + n_4 + n_5 \quad (21)$$

is obeyed. The symbol $\rho^{(n)}(2)$ represents the two-node contribution to the $2n$ th moment. The quantum statistical average in Eq. (19) is with respect to the full Hamiltonian in Eq. (A4). The contribution of the second two-node graph in Fig. 4(c) is given by

$$\rho^{(n)}(2)_2 = 2 \sum_{\{n\}} (2K)^{2n_1+2n_3+2} [1 - (-1)^{n_2}] \sum_j C_j^2 \omega_j^{n_2} \quad (22)$$

with the constraint

$$2n = 4 + 2n_1 + n_2 + 2n_3. \quad (23)$$

The above constraint requires n_2 to be an even integer and from Eq. (22) we find that the factor $1 - (-1)^{n_2}$ yields a zero contribution for this graph. Thus, the entire two-node contribution is given by Eq. (19). Although the contribution in Eq. (22) is zero at the two-node level, we find that the graphical structure does contribute as unlinked pieces in higher-node graphs. We address this issue in Eq. (27).

In obtaining the graph in Fig. 4(c) it is useful to explain the origin of the loop between the nodes. Consider first the case in which there is no circle on the line of the loop. The left-hand node is the second graphical element in Fig. 1(b) and corresponds to the contribution

$$2 \sum_j C_j (a_j(t) + a_j^\dagger(t)) \sigma_x(t).$$

We next take the time derivative of the bath operators in the above expression and pick up the second graphical contribution in Figs. 1(d) and 1(e). The expression becomes

$$2[(-1)^1 + 1] \sum_j C_j^2 \sigma_z(t) \sigma_x(t).$$

Using Eq. (A10a), the expression reduces to

$$2[(-1)^1 + 1] \sum_j C_j^2 \bar{\sigma}_y(t).$$

Thus, the collapse of two spin operators to one closes the loop and leaves the spin operator $\bar{\sigma}_y(t)$ as seen from the labeling of the lines in Fig. 4(c). If we include higher derivatives which produce circles on the loop lines, in particular n_2 of them, the expression above becomes

$$2[(-1)^{n_2+1} + 1] \sum_j C_j^2 \omega_j^{n_2} \bar{\sigma}_y(t).$$

Loop structures are common in the spin-boson graphs and occur from the collapse of two spin operators to one. Whenever possible, we always carry out the collapse.

For the three-node graphs we find that it is again impossible to construct a graph which ends up with a nonzero canonical average of operators. Thus, the contribution of the three-node graphs is zero. To display the four-node graphs, we first simplify the graph notation. We note in Fig. 4 that all dashed lines in the graphs always have circles on them. By convention we assume that the circles become part of the lines and we call such graphs the simplified graphs. In Fig. 5 we present the simplified four-node graphs. We forego an explicit enumeration of all the graphs since they are obtained in a straightforward manner from the rules described above as displayed in the evaluation of the graphs in Fig. 4. We refer also to our previous work on related graphs.²⁰

We turn next to the issue of evaluating the thermal averages of the bath operators. In the present work we follow

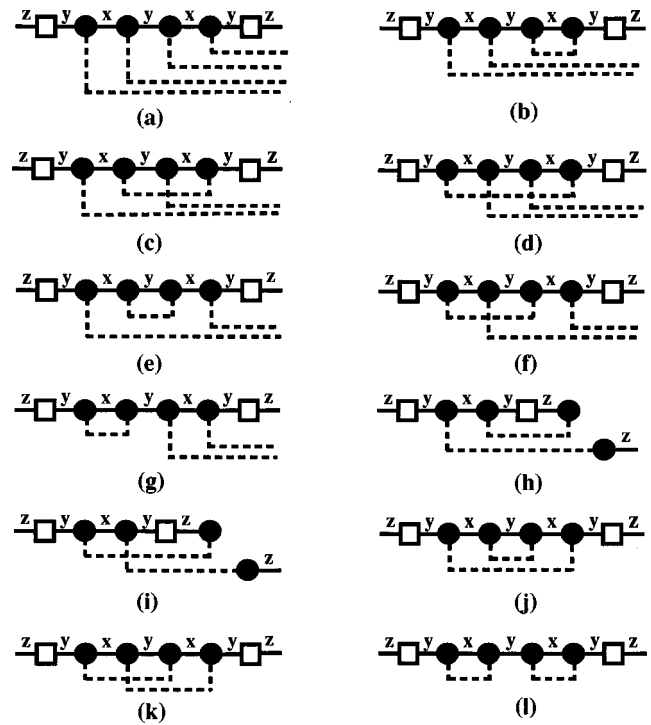


FIG. 5. Simplified four-node graphs.

the prescription described in our previous work and evaluate the averages by a suitable expansion as described in Appendix B. In the lowest order we replace the full thermal average $\langle \cdots \rangle$ by an average over the bath Hamiltonian given by

$$H_B = \sum_j \omega_j a_j^\dagger a_j \quad (24)$$

in reduced units. A more complete explanation of the approximate thermal averages is given in Appendix B. We denote the bath average by the symbol $\langle \cdots \rangle_0$. Based on this approximate scheme for the thermal averages, the leading contribution to the two-node graph in Fig. 4(b) and Eq. (19) is given by

$$\rho^{(n)}(2,2) = 4K^2 \sum_{\{n\}} (2K)^{n_1} (n_1 + 1) L^{(2)}(n_2) \quad (25)$$

with the constraint

$$2n = 4 + n_1 + n_2 \quad (26)$$

with both n_1 and n_2 even integers and where

$$L^{(2)}(m) = 4[(1 + (-1)^m)g_{m+1} + (-1)^m f_{m+2}] + 2[1 - (-1)^m]f_{m+2} \quad (27)$$

and the functions f_n and g_n are defined in Appendix C. In the symbol $\rho^{(n)}(k,m)$ the index k represents the number of nodes in the graph and the index m represents the maximum level of the linked piece. Note that the second term is a zero contribution in Eq. (27) since $m = n_2$ is even. This piece comes from Eq. (22) and the graph in Fig. 4(c).

We have specifically written the algebraic form in Eq. (25) to display the leading term in an unlinked expansion. This concept has been described in detail previously by us.²⁰

In particular, using the bath average approximation, the contribution of the four-node graphs in Fig. 5 can be written as

$$\begin{aligned} \rho^{(n)}(4,4) = & \sum_{\{n\}} (4K^2)^{n_1+1} (n_1+1) L^{(4)}(n_2) \\ & + \sum_{\{n\}} (4K^2)^{n_1+1} [n_1+2] L^{(2)}(n_2) L^{(2)}(n_3) \end{aligned} \quad (28)$$

with the constraint

$$2n = 6 + 2n_1 + n_2 \quad (29)$$

on the first term and

$$2n = 6 + 2n_1 + n_2 + n_3 \quad (30)$$

on the second term, and where

$$\begin{aligned} L^{(4)}(m) = & 16 \sum_{\{n\}} (4K^2)^{n_1} [2n_1, n_3, n_4] \{ [g_{n_2+n_4+1} + (-1)^{n_2+n_4} (g_{n_2+n_4+1} + f_{n_2+n_4+2})] \\ & \times [g_{n_3+n_6+1} + (-1)^{n_3+n_6} (g_{n_3+n_6+1} + f_{n_3+n_6+2})] + [g_{n_2+n_4+n_6+1} + (-1)^{n_2+n_4+n_6} (g_{n_2+n_4+n_6+1} + f_{n_2+n_4+n_6+2})] \\ & \times [g_{n_3+1} + (-1)^{n_3} (g_{n_3+1} + f_{n_3+2})] \} + \sum_{\{n\}} (4K^2)^{n_1} [2n_1, n_3, n_4] \{ 8[1 - (-1)^{n_3+n_5}] f_{n_3+n_5+2} \\ & \times [g_{n_2+n_4+1} + (-1)^{n_2+n_4} (g_{n_2+n_4+1} + f_{n_2+n_4+2})] + 8[1 - (-1)^{n_2+n_3+n_5}] f_{n_2+n_3+n_5+2} \\ & \times [g_{n_4+1} + (-1)^{n_4} (g_{n_4+1} + f_{n_4+2})] + 8[1 - (-1)^{n_3}] f_{n_3+2} [g_{n_2+n_4+n_5+1} + (-1)^{n_2+n_4+n_5} \\ & \times (g_{n_2+n_4+n_5+1} + f_{n_2+n_4+n_5+2})] + 8[1 - (-1)^{n_2+n_3}] f_{n_2+n_3+2} [g_{n_4+n_5+1} + (-1)^{n_4+n_5} (g_{n_4+n_5+1} + f_{n_4+n_5+2})] \\ & + 4[1 - (-1)^{n_3}] [1 - (-1)^{n_2+n_4+n_5}] f_{n_3+2} f_{n_2+n_4+n_5+2} + 4[1 - (-1)^{n_2+n_3}] [1 - (-1)^{n_4+n_5}] f_{n_2+n_3+2} f_{n_4+n_5+2} \} \\ & + \sum_{\{n\}} (4K^2)^{n_1} [2n_1+1, n_3, n_4] \{ 4[1 - (-1)^{n_3}] [1 - (-1)^{n_2+n_4+n_5}] f_{n_3+2} f_{n_2+n_4+n_5+2} \\ & + 4[1 - (-1)^{n_2+n_3}] [1 - (-1)^{n_4+n_5}] f_{n_2+n_3+2} f_{n_4+n_5+2} \}. \end{aligned} \quad (31)$$

In the first term of Eq. (31) we have the constraint

$$m = 2n_1 + \sum_{j=1}^6 n_j \quad (32)$$

and

$$m = 2n_1 + \sum_{j=1}^5 n_j \quad (33)$$

in the remaining terms. As can be seen, the contribution in Eq. (28) comes from four-node graphs with two-node and four-node linked pieces. Comparing the second term in Eq. (28) with Eq. (27) as well as comparing the underlying graphs, it is clear that the unlinked two-node contribution of graphs with a higher number of nodes can be used to compute contributions to time derivatives having the structure of the two-node graphs in Figs. 4(b) and 4(c). Algebraically, we denote these contributions as

$$\begin{aligned} \rho^{(n)}(2)_u = & \sum_{q=1}^n \sum_{\{n\}} (4K^2)^{n_1+1} [n_1, q] \prod_{j=1}^q L^{(2)}(n_{j+1}) \\ = & \sum_{q=1}^n \rho^{(n)}(2q, 2) \end{aligned} \quad (34)$$

with the constraint

$$2n = 2 + 2q + 2n_1 + \sum_{i=2}^{q+1} n_i. \quad (35)$$

Further examination of Eq. (28) shows that the first term is equivalent in structure to Eq. (25) except that the linked four-node piece replaces the linked two-node piece. This structure permits us to include linked four-node pieces in higher-node graphs. In summary we find algebraically that

$$\begin{aligned} \rho^{(n)}(4)_u = & \sum_{\{p,q\}} \sum_{\{n\}} (4K^2)^{n_1} [n_1, p+q] [p, q] \\ & \times \prod_{j=2}^{p+1} L^{(4)}(n_j) \prod_{k=p+2}^{p+q+1} L^{(2)}(n_k) \end{aligned} \quad (36)$$

with the constraint

$$2n = 2 + 4p + 2q + 2n_1 + \sum_{i=2}^{p+q+1} n_i. \quad (37)$$

Although the notation in Eq. (36) is complicated, implementation is straightforward. Let us summarize what the result in Eq. (36) accomplishes. At the lowest level of the bath approximation for the thermal average, $\langle \cdots \rangle_0$, this equation includes the contributions to the $2n$ th time derivative from the graphs in Figs. 4(b), 4(c) and 5 as well as the unlinked two-node and four-node pieces from higher-node graphs

which have the structure evident in these figures. We have shown in previous work that this many-node, unlinked strategy is a useful computational approximation for computing higher time derivatives at the four-node linked level.²⁰

For the zero temperature case we have worked out the linked contributions from the six-node graphs. We forgo a display of these graphs and the resulting algebraic formula for $L^{(6)}(m)$ since there are 104 graphs and the formula is lengthy. At zero Kelvin the linked six-node pieces are included using the formula

$$\begin{aligned} \rho^{(n)}(6)_u = & \sum_{\{r,p,q\}} \sum_{(n)} (4K^2)^{n_1} [n_1 + r + p + q, r + p + q] \\ & \times [r, p, q] \prod_{i=2}^{r+1} L^{(6)}(n_i) \prod_{j=r+2}^{r+p+1} L^{(4)}(n_j) \\ & \times \prod_{k=r+p+2}^{r+p+q+1} L^{(2)}(n_k) \end{aligned} \quad (38)$$

with the constraint

$$2n = 2 + 6r + 4p + 2q + 2n_1 + \sum_{j=2}^{r+p+q+1} n_j. \quad (39)$$

We conclude our discussion of the graphical evaluation of time derivatives or moments by summarizing the many-node, unlinked approach at the four-node level since this is the basis for most of our computations. We first evaluate the contributions of the two-node and four-node linked pieces using Eq. (36). We then evaluate the next higher-order contribution from the thermal average of Fig. 4(b) as described in Appendix B. We call this approach the four-node computation since all linked contributions through four nodes are calculated. Since this approach is based on an approximate evaluation of time derivatives, we expect that there will be parameter regimes for choices of α , K , and β in the spin-boson model for which the evaluation process breaks down. We consider this point in Sec. IV.

We point out that other methods are available to compute the required time derivatives or moments. In particular for the spin-boson case Stockburger and Mak⁵⁶ have developed an exact path integral solution which could be used. For the present work we use the graphical procedure since we want to explore its potential utility.

III. MAXIMUM ENTROPY IMAGING

In a companion paper²³ we have described the use of a maximum entropy imaging process based on the moments of a spectral density. In the present work we focus on imaging of the spectral density $\rho(\omega)$ in Eq. (2) since it is most directly related to the time correlation function of interest. The polynomial maxent imaging (Pmaxent) process^{23,62,63} used herein is based on maximization of the information entropy S given by

$$S = - \int_{\omega_a}^{\omega_b} d\omega \rho(\omega) \ln \frac{\rho(\omega)}{em(\omega)} + \sum_{m=0}^M \lambda_m (\bar{\tau}^{(m)} - \tau^{(m)}), \quad (40)$$

where

$$\tau^{(m)} = \int_{\omega_a}^{\omega_b} d\omega Q_m(\omega^2) \rho(\omega), \quad (41)$$

$$Q_m(\omega^2) = \frac{\prod_{i=0, i \neq m}^M (\omega^2 - \omega_i^2)}{\prod_{i=0, i \neq m}^M (\omega_m^2 - \omega_i^2)}, \quad (42)$$

M is the number of known moments of $\rho(\omega)$ other than normalization, and the frequencies ω_i are defined by

$$\omega_i = \frac{\omega_b - \omega_a}{2} x_i + \frac{\omega_b + \omega_a}{2}, \quad (43)$$

where

$$x_i = \cos \frac{2i+1}{2M+2} \pi; \quad i = 0, 1, \dots, M. \quad (44)$$

The polynomials $Q_m(\omega^2)$ are Lagrange interpolation polynomials. The term $\bar{\tau}^{(m)}$ is defined by Eq. (41) with the spectral density given by the image of $\rho(\omega)$ instead of the exact result. The exact moments $\tau^{(m)}$ in Eq. (41) are easily computed from the standard moments $\rho^{(n)}$ obtained in the previous section by substitution of Eq. (42) into Eq. (41). The function $m(\omega)$ is a default distribution which in the present work is taken to be uniform. Maximization of the entropy functional in Eq. (40) with the coefficients λ_m taken as Lagrange multipliers yields the analytic image

$$\rho(\omega) = m(\omega) \exp \left(\sum_{m=0}^M \lambda_m Q_m(\omega^2) \right). \quad (45)$$

To find the coefficients λ_m , we next minimize the dual space function Y given by

$$Y = \int_{\omega_a}^{\omega_b} d\omega m(\omega) \exp \left(\sum_{m=0}^M \lambda_m Q_m(\omega^2) \right) - \sum_{m=0}^M \lambda_m \tau^{(m)} \quad (46)$$

in the space of the coefficients λ_m . The details of this minimization process and the advantages of using the Lagrange interpolation polynomials are described elsewhere.^{23,62,63}

The end points of the integration ω_a and ω_b are also parameters which must be obtained. In the present work we compute the information entropy S as a function of ω_a and ω_b using the process described above and search for the maximum in S using a random walk on ω_a and ω_b . Details of this process are presented in our companion paper on the Pmaxent process.²³

Finally, we obtain the Pmaxent image of $C(t)$ by inverting the Fourier transform using Eq. (5) where the integral is computed numerically using an 80-point Gauss–Legendre quadrature.⁶⁴

IV. RESULTS

We present in this section the results of computations on the spin-boson time correlation function $C(t)$ given in Eq. (10). Our approach is to compute time derivatives using the four-node graphical method described in Sec. II and to process these derivatives with the Pmaxent method of Sec. III.

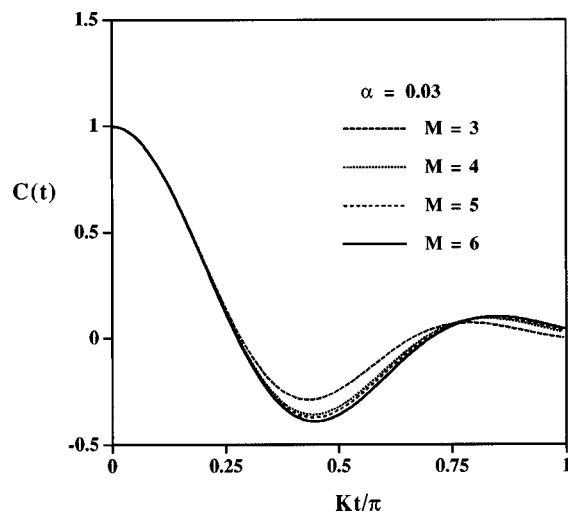


FIG. 6. Convergence of $C(t)$ as a function of number of time derivatives M for $\alpha=0.03$, $K=0.4$, and $\beta=0.25$ in reduced units.

A. Comparison with dynamical path-integral Monte Carlo

Following Mak and Chandler,³⁵ we begin with the parameter regime $K=0.4$ and vary α and β . In Fig. 6 we first examine convergence as a function of the number of time derivatives for $\alpha=0.03$ and $\beta=0.25$. We find that $C(t)$ is well converged by $M=6$. A similar level of convergence at $M=6$ is found for all cases with $K=0.4$. We point out that the total computation time using an IBM6000-320H is approximately 1 min for each curve in Fig. 6.

A special feature of our method is that the Fourier transform $\rho(\omega)$ of $C(t)$ is directly obtained through Eq. (45). In Fig. 7 we examine convergence of $\rho(\omega)$ as a function of the number of time derivatives and we again see satisfactory convergence at $M=6$.

As described in the Introduction, the coherent-incoherent boundary is of special interest in the spin-boson model. To find this boundary for fixed K and β , we search for the value of α where $C(t)$ ceases to oscillate in time and dies monotonically to zero. In Figs. 8 and 9 we present $C(t)$

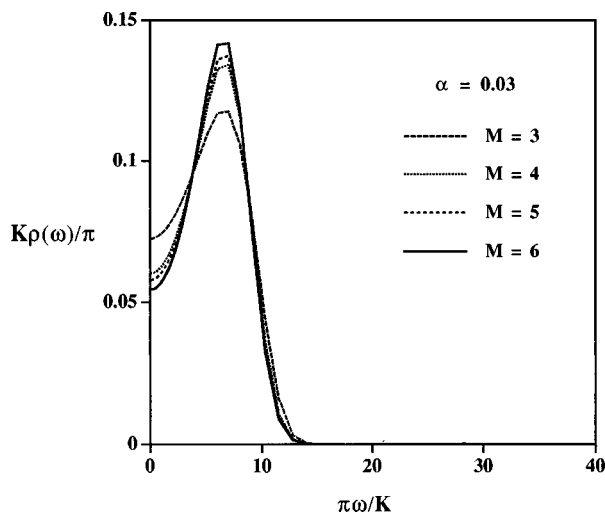


FIG. 7. Same as Fig. 6 for spectral density $\rho(\omega)$.

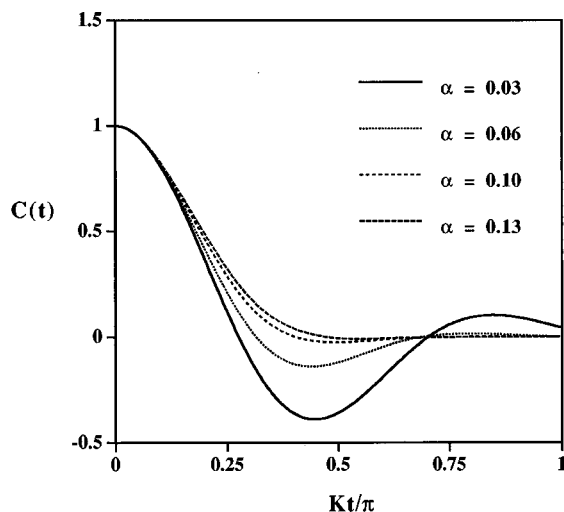


FIG. 8. Crossover of $C(t)$ from coherent to incoherent decay as a function of α for $K=0.4$ and $\beta=0.25$ with $M=6$.

and the corresponding $\rho(\omega)$ as a function of α for $K=0.4$ and $\beta=0.25$. We find that the coherent-incoherent boundary occurs between $\alpha=0.06$ and $\alpha=0.10$. The curves for $C(t)$ in Fig. 8 are very similar to the ones reported by Mak and Chandler. The shape of the curves in Fig. 9 for $\rho(\omega)$ around $\omega=0$ are also of interest. We see that the coherent-incoherent boundary corresponds approximately to the switchover from a positive initial derivative to a negative derivative. From our work on the linear chain Hamiltonian,²³ we know that computation of $\rho(0)$ is especially difficult using moment imaging methods. We further know that the value $\rho(0)$ affects the coherent-incoherent boundary in a sensitive way since the negative dip in $C(t)$ is influenced by $\rho(0)$. It is interesting to see that the boundary is reasonably well obtained in this case.

An important parameter regime which is available to our approach but which is difficult for path integral approaches is the case at $T=0$ K. In Figs. 10 and 11 we show results for $C(t)$ and the corresponding $\rho(\omega)$ at $M=6$, $K=0.4$, and $T=0$ K as a function of α using the six-node level of compu-

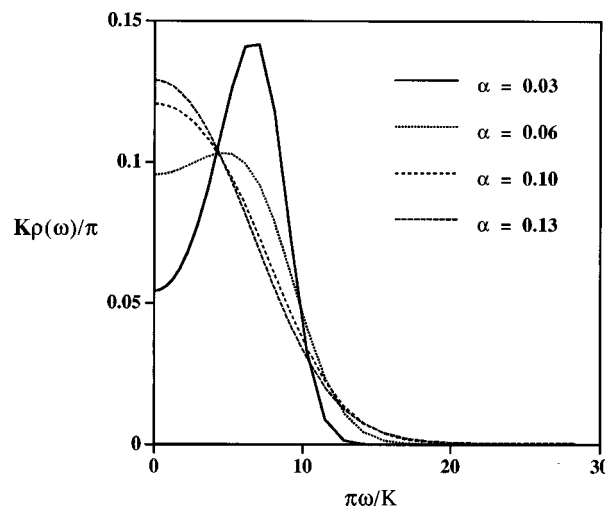


FIG. 9. Same as Fig. 8 for spectral density $\rho(\omega)$.

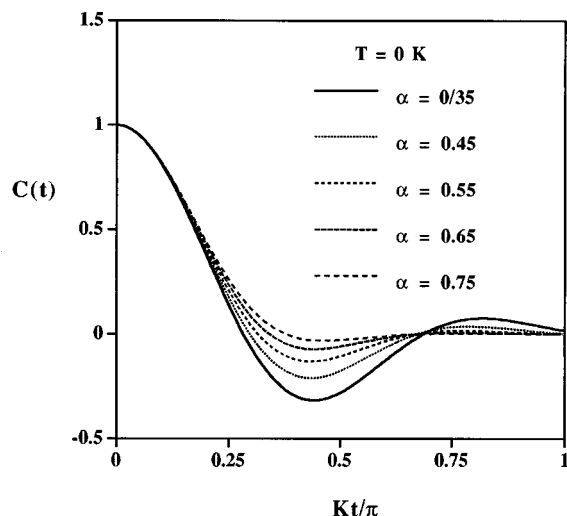


FIG. 10. Crossover of $C(t)$ from coherent to incoherent decay at a temperature of 0 K as a function of α for $K=0.04$ with $M=6$.

tation. We find the six-node and four-node results to be in close agreement with the dominant affect being the number of moments used. Close inspection of the data for $C(t)$ shows that the coherent–incoherent boundary occurs between $\alpha=0.65$ and $\alpha=0.75$. Again, we note the behavior of $\rho(\omega)$ around $\omega=0$ and the strong correlation between the shape of the spectral density and the coherent–incoherent boundary.

For the case $K=0.4$ we show in Fig. 12 the coherent–incoherent boundary. Coherent decay is shown by solid circles and incoherent decay by open diamonds. The noninteracting blip approximation^{27,32,60} for the boundary line is shown by a solid line. In all essential respects our results are in substantial agreement with the path integral results of Mak and Chandler for $K=0.4$. We also find for 0 K that the boundary is located at larger values of α than the value of 0.5 found from the noninteracting blip approximation and from Stockburger and Mak⁶¹ using a new quantum Monte Carlo method in the limit of large cutoff frequency ω_c . Since our

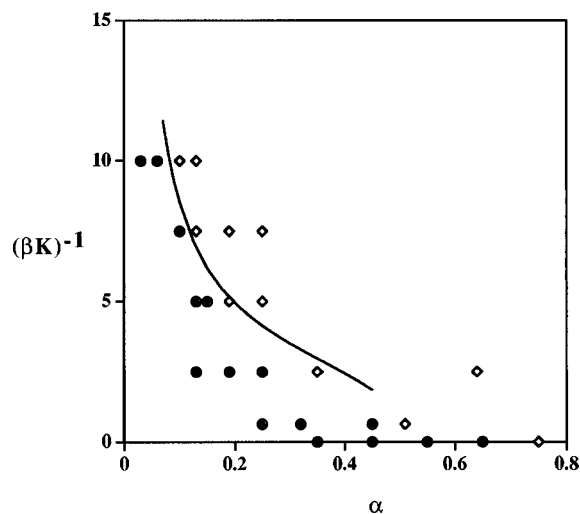


FIG. 12. Coherent (solid circles)–incoherent (open diamonds) boundary at $K=0.4$ compared with noninteracting-blip approximation (solid line).

results are scaled by ω_c , the direct dependence of ω_c is not immediately available to check the behavior at large ω_c . In particular with a K value of 0.4 we are in the regime of intermediate ω_c as compared to the values in Stockburger and Mak.⁶¹ We pursue the dependence on ω_c elsewhere. Furthermore, we have found that the TCF images in Fig. 10 can be changed somewhat, including the dip below zero, by adjusting the value of $\rho(\omega)$ at $\omega=0$ while maintaining agreement with the moments; that is, the dip is sensitive to the value $\rho(0)$. Viewed from a different perspective, we find that convergence of $\rho(\omega)$ at $\omega=0$ using moment information can be slow in some cases since the moments themselves are sometimes not very sensitive to $\rho(\omega)$ near $\omega=0$. This behavior of Pmaxent images is currently under study.

We next consider the situation at larger values of α . In Fig. 13 we present $C(t)$ for $\alpha=1.27$, $K=0.4$, and $(\beta K)^{-1}=0.625$ with $M=5$ and $M=6$. The result is not strongly dependent on the number of moments M . Mak and Chandler find a similar decay but with $C(t)$ having a value slightly below 0.5 at $Kt/\pi=1$. This disagreement is due to the ex-

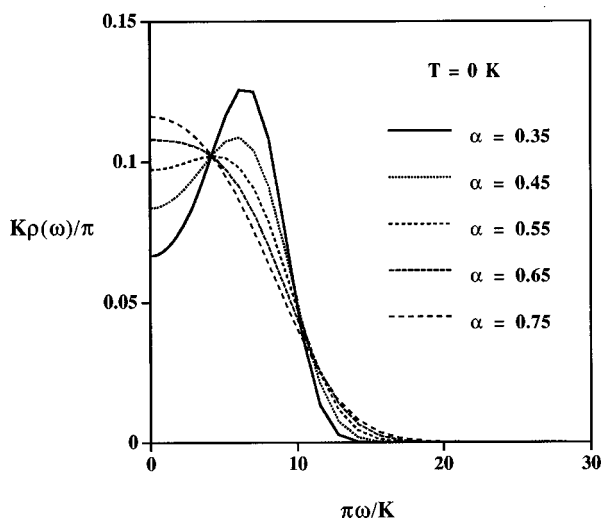


FIG. 11. Same as Fig. 10 for spectral density $\rho(\omega)$.

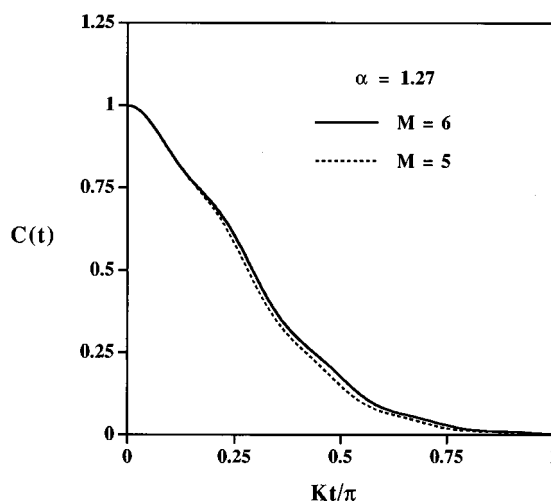
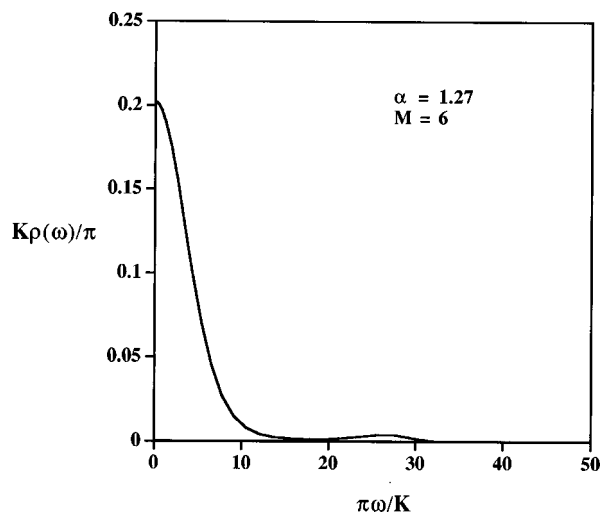


FIG. 13. Decay of $C(t)$ at $\alpha=1.27$, $K=0.4$, and $(\beta K)^{-1}=0.625$.

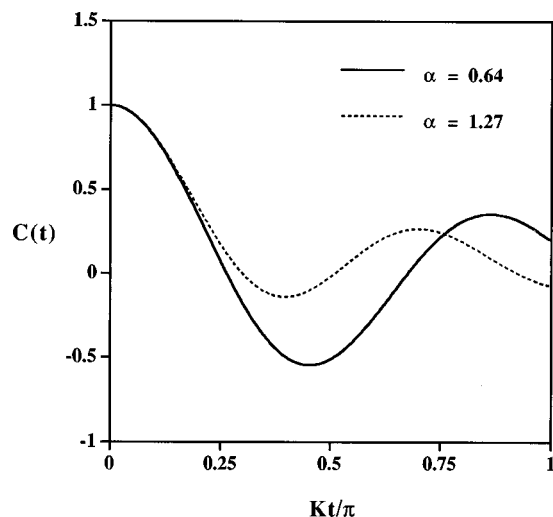
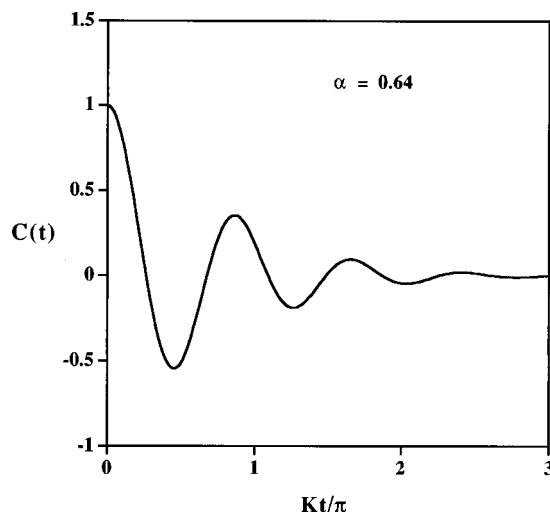
FIG. 14. Same as Fig. 13 for spectral density $\rho(\omega)$.

pected breakdown in our perturbative approach with respect to α or number of nodes of evaluating the thermal averages which appear in the graphical contributions. In Fig. 14 we show the spectral density $\rho(\omega)$ for this case. The peak at $\pi\omega/K=30$ is the origin of the small oscillations in $C(t)$ and is probably an artifact of the approximate time derivatives.

In Fig. 15 we examine $C(t)$ for the case $K=1.6$ and $(\beta K)^{-1}=0.625$ with $\alpha=0.64$ and $\alpha=1.27$. With the value of K increased we find that we are able to achieve converged results for larger values of α . In particular results for both $\alpha=0.64$ and $\alpha=1.27$ are in agreement with Mak and Chandler. We have attempted to obtain results at $\alpha=2.55$ but find the expected breakdown at large α in our method.

As pointed out by Mak and Chandler, the results in Fig. 15 indicate that coherence is maintained for $\alpha \gg 0.5$, whereas the noninteracting-blip approximation predicts that coherence will cease at $\alpha=0.5$. We confirm their findings on this point.

We have attempted computations in the deep tunneling limit of large α , large β , and small K but find unsatisfactory

FIG. 15. Decay of $C(t)$ at $\alpha=0.64$ and $\alpha=1.27$, $K=1.6$, and $(\beta K)^{-1}=0.625$.FIG. 16. Long-time decay of $C(t)$ for $\alpha=0.64$, $K=1.6$, and $(\beta K)^{-1}=0.625$.

convergence due to the form of the expansion for computing thermal averages. At the present time we do not believe the failure of moment imaging in this regime is due to the imaging process itself but rather to poorly computed moments. We are presently working to improve these computations.

B. Long-time behavior

A major problem at present in quantum dynamical simulations is the need for simulation methodologies which permit computations at longer times.^{1,6} The graphical Pmaxent approach described herein is one possible solution to this problem. To illustrate this conjecture, we display in Fig. 16 the curve for $C(t)$ for $\alpha=0.64$ in Fig. 15 to longer times. Here, $K=1.6$ and $(\beta K)^{-1}=0.625$. We find as expected that dissipation from the bath results in oscillatory decay of $C(t)$ to zero at long time. Similar results at long-time for $C(t)$ can be obtained for any choice of parameters for which convergence with respect to number of moments is achieved. In previous work on other systems we have demonstrated similar well behaved results at long time.^{16,18} We conclude that the graphical Pmaxent approach is capable of producing the behavior of time correlation functions at longer times.

C. Direct computation of decay time

The decay time of a time correlation function can often be obtained from the relation

$$\tau = \frac{\pi}{2} \rho(0) = \int_0^\infty dt C(t). \quad (47)$$

We discuss this relation in the context of MTGLE in Appendix D. In terms of the graphical Pmaxent approach, the value $\rho(0)$ is directly available computationally. In Table I we present values of τ computed using Eq. (47) for the case $K=0.4$, $\beta=0.25$, and various values of α . These decay times can be compared with the TCF curves in Fig. 8. As one would expect, these values do not provide the decay of the oscillations in the coherent regime where $\alpha=0.03$ and $\alpha=0.06$. On the other hand, in the incoherent regime of

TABLE I. Decay time for $C(t)$ with $K=0.4$, $\beta=0.25$, and $M=6$.

α	$K\tau/\pi$
0.03	0.097
0.06	0.164
0.10	0.203
0.13	0.217

$\alpha=0.10$ and $\alpha=0.13$, the decay times of 0.203 and 0.217 are consonant with decay to e^{-1} of the initial value and correctly show that the decay curve for $\alpha=0.13$ has a slightly larger decay time than the one for $\alpha=0.10$. We point out that the curves are not pure exponential decay following the initial quadratic decay in time. We have verified this point by examining logarithmic plots which are found to show small curvature at longer times. We conclude that the graphical Pmaxent approach provides a direct measure of the decay time in the incoherent regime using Eq. (47).

V. SUMMARY AND CONCLUSIONS

The computation of quantum time correlation functions at both short and long times and over a wide range of temperature for condensed phase systems is an important goal. Herein, in the context of the spin-boson model, we have shown that the graphical Pmaxent approach shows considerable promise in this regard. In particular within the limits of the methodology used to compute the time derivatives of the TCF or alternatively the moments of its spectral density, we have shown agreement with the dynamical path-integral Monte Carlo results of Mak and Chandler³⁵ with respect to the coherent–incoherent boundary. We have shown that the graphical Pmaxent is stable both at long time and low temperature. A special feature of the approach is the ability to directly compute the decay time in the incoherent regime from the spectral density at zero frequency.

The fundamental idea of the graphical Pmaxent approach is that the early time derivatives of the TCF or the moments of its spectral density contain sufficient information, if properly processed, to allow for computation of the TCF in a systematic manner. This idea is by no means new and was pioneered by Gordon^{65,66} and considered by Berne and Harp in a context similar to that described herein.⁶⁷ Furthermore, the use of maximum entropy imaging of $\rho(\omega)$ per se is not new with many variations extant but its use to image TCFs has been limited.^{66–85} The Pmaxent method presented here is a relatively new and powerful imaging approach. Furthermore, the graphical process introduced elsewhere by us allows for a compact characterization of the structure of the moments.²⁰ At the present time, we have computed the thermal averages required for the moments using a perturbation approach. We point out that these moments could in principle be computed exactly using an equilibrium path-integral method.⁵⁶ Such an approach would provide a stronger test of the fundamental idea.

ACKNOWLEDGMENT

We thank the Robert A. Welch Foundation, Grants Nos. Y-1234 and Y-1303, for their support of this research.

APPENDIX A: DIMENSIONAL REDUCTION OF HAMILTONIAN

The standard spin-boson Hamiltonian in Eq. (6) can be transformed to second-quantized form using the expansion of x_j in terms of standard annihilation and creation operators given by

$$x_j = \left(\frac{\hbar}{2m_j\omega_j} \right)^{1/2} (a_j + a_j^\dagger). \quad (\text{A1})$$

One obtains

$$H = -K\sigma_x + \sum_j \hbar\omega_j \left(a_j^\dagger a_j + \frac{1}{2} \right) + \sum_j C_j \left(\frac{\hbar}{2m_j\omega_j} \right)^{1/2} (a_j + a_j^\dagger) \sigma_z. \quad (\text{A2})$$

The cutoff frequency ω_c can be used to define dimensionless parameters given by

$$H^* = \frac{H}{\hbar\omega_c}, \quad (\text{A3a})$$

$$t^* = \omega_c t, \quad (\text{A3b})$$

$$\beta^* = \hbar\omega_c\beta, \quad (\text{A3c})$$

$$K^* = \frac{K}{\hbar\omega_c}, \quad (\text{A3d})$$

$$\omega_j^* = \frac{\omega_j}{\omega_c}, \quad (\text{A3e})$$

and

$$C_j^* = \frac{C_j}{\hbar\omega_c} \left(\frac{\hbar}{2m_j\omega_j} \right)^{1/2}, \quad (\text{A3f})$$

where t is the time. With these dimensionless parameters the Hamiltonian is given by

$$H^* = -K^*\sigma_x + \sum_j \omega_j^* a_j^\dagger a_j + \sum_j C_j^* (a_j + a_j^\dagger) \sigma_z. \quad (\text{A4})$$

We ignore the usual zero-point energy term since it plays no role.

The spectral distribution $J(\omega)$ in Eqs. (8) and (9) can be reformulated in terms of reduced variables and is given by

$$\sum_j (C_j^*)^2 \delta(\omega^* - \omega_j^*) = \frac{\alpha}{2} \omega^* e^{-\omega^*}, \quad (\text{A5})$$

where α is a dimensionless parameter given by

$$\alpha = \frac{2\eta}{\hbar\pi}. \quad (\text{A6})$$

With $\hbar=1$, this definition of α allows us to make contact with the parameter values used by Mak and Chandler.³⁵ From Eq. (A5) it is easy to see that

$$\sum_j (C_j^*)^2 f(\omega_j^*) = \frac{\alpha}{2} \int_0^\infty d\omega^* \omega^* e^{-\omega^*} f(\omega^*), \quad (\text{A7})$$

where $f(\omega)$ is typically a power of ω . This integral representation is the basis for the calculation of terms involving the coupling coefficients which arise in our computations. When required we integrate using a 68-point Laguerre quadrature. In the text of the paper for Secs. II–V, we drop the starred notation for convenience. The reader should assume that all quantities are scaled as described above.

Some useful properties of the spin operators σ_x , $\bar{\sigma}_y$, and σ_z are

$$\sigma_x^2 = \sigma_z^2 = -\bar{\sigma}_y^2 = 1, \quad (\text{A8})$$

$$\{\sigma_x, \sigma_z\} = \{\bar{\sigma}_y, \sigma_z\} = \{\sigma_x, \bar{\sigma}_y\} = 0, \quad (\text{A9})$$

$$\sigma_x \sigma_z = -\sigma_z \sigma_x = -\bar{\sigma}_y, \quad (\text{A10a})$$

$$\bar{\sigma}_y \sigma_z = -\sigma_z \bar{\sigma}_y = -\sigma_x, \quad (\text{A10b})$$

and

$$\sigma_x \bar{\sigma}_y = -\bar{\sigma}_y \sigma_x = -\sigma_z. \quad (\text{A10c})$$

APPENDIX B: THERMAL AVERAGES

Following our analysis of thermal averages in previous work,²⁰ we define

$$H = H_0 + V, \quad (\text{B1})$$

$$H_0 = -K\sigma_x + H_B, \quad (\text{B2})$$

and

$$V = \sum_j C_j (a_j + a_j^\dagger) \sigma_z, \quad (\text{B3})$$

with H_B given in Eq. (24). We further define the partition functions

$$Q = \text{Tr } e^{-\beta H} \quad (\text{B4})$$

and

$$Q_0 = \text{Tr } e^{-\beta H_0}, \quad (\text{B5})$$

where $\beta = (kT)^{-1}$. The exponential $e^{-\beta H}$ is then expanded such that

$$\begin{aligned} e^{-\beta H} &= e^{-\beta H_0} - \int_0^\beta d\beta_1 e^{-(\beta-\beta_1)H_0} V e^{-\beta_1 H_0} \\ &\quad + \int_0^\beta d\beta_1 e^{-(\beta-\beta_1)H_0} V \\ &\quad \times \int_0^{\beta_1} d\beta_2 e^{-(\beta_1-\beta_2)H_0} V e^{-\beta_2 H_0} + \dots \end{aligned} \quad (\text{B6})$$

For some general operator A we can write its statistical average as

$$\langle A \rangle = \frac{\frac{1}{Q_0} \text{Tr } e^{-\beta H} A}{\frac{1}{Q_0} \text{Tr } e^{-\beta H}}. \quad (\text{B7})$$

To evaluate Eq. (B7), we evaluate both numerator and denominator using the expansion in Eq. (B6). For convenience of notation we use

$$\langle A \rangle_0 = \frac{1}{Q_0} \text{Tr } e^{-\beta H_0} A. \quad (\text{B8})$$

Then, making implicit use of Eqs. (B5) and (B6), we write

$$\frac{1}{Q_0} \text{Tr } e^{-\beta H} A = A_n + A_{n+2} + A_{n+4} + \dots \quad (\text{B9})$$

and

$$\frac{1}{Q_0} \text{Tr } e^{-\beta H} = 1 + Q_2 + Q_4 + \dots, \quad (\text{B10})$$

where the subscript on A and Q indicates order of magnitude in the nonlinear interaction or number of integrals in Eq. (B6). We note that only an even number of interactions V occur since the number of quanta in the oscillator bath is preserved in the trace. We assume in Eq. (B9) that the expansion does not necessarily start at $n=0$, but at some larger value n . Then we have from Eq. (B6) that

$$\begin{aligned} \langle A \rangle &= A_n + (A_{n+2} - Q_2 A_n) \\ &\quad + [A_{n+4} - Q_2 A_{n+2} + A_n (Q_2^2 - Q_4)] + \dots \end{aligned} \quad (\text{B11})$$

The advantage of Eq. (B11) over Eq. (B7) is that all terms of the same order of magnitude are collected together.

As a particular example of this evaluation process, we find that Q_2 is given by

$$\begin{aligned} Q_2 &= \int_0^\beta d\beta_1 \int_0^{\beta_1} d\beta_2 \left[\frac{e^{(\beta-2\beta_1+2\beta_2)K} + e^{-(\beta-2\beta_1+2\beta_2)K}}{e^{\beta K} + e^{-\beta K}} \right] \\ &\quad \times \sum_j C_j^2 \{ e^{\omega_j(\beta_2-\beta_1)} [n(\omega_j) + 1] \\ &\quad + e^{\omega_j(\beta_1-\beta_2)} n(\omega_j) \}, \end{aligned} \quad (\text{B12})$$

where

$$n(\omega_j) = \frac{1}{e^{\beta\omega_j} - 1}. \quad (\text{B13})$$

The integrals can be evaluated as required.

At the four-node level the only higher-order statistical average which must be evaluated is found in the two-node graph given by the expression in Eq. (19). Thus, we must compute the diagram contribution given by

$$\begin{aligned} &4 \sum_{\{n\}} (2K)^{2n_1+2n_3+2} [2n_3+1, n_4, n_5] \sum_{jk} C_j C_k \omega_j^{n_2+n_5} \omega_k^{n_4} \\ &\quad \times \{ \langle [(-1)^{n_2+n_5} a_j + a_j^\dagger] [(-1)^{n_4} a_k + a_k^\dagger] \rangle_2 \\ &\quad - Q_2 \langle [(-1)^{n_2+n_5} a_j + a_j^\dagger] [(-1)^{n_4} a_k + a_k^\dagger] \rangle_0 \}. \end{aligned}$$

To carry out this computation, we evaluate the statistical average using the process described above, convert the sums on j and k to integrals following the prescription in Eq. (A10), and numerically evaluate the term using a 68-point

Laguerre quadrature. We forego an explicit display of the final expression since it is complicated but otherwise obtainable by simple manipulation as described.

APPENDIX C: ADDITIONAL FUNCTIONS

The functions f_n and g_n are defined such that

$$f_{n+2} = \sum_j C_j^2 \omega_j^n = \frac{\alpha}{2} \int_0^\infty d\omega \omega^{n+1} e^{-\omega} = \frac{\alpha}{2} (n+1)! \quad (\text{C1})$$

and

$$g_{n+1} = \sum_j C_j^2 \omega_j^n \langle a_j^\dagger a_j \rangle_0 = \frac{\alpha}{2} \int_0^\infty d\omega \frac{\omega^{n+1} e^{-\omega}}{e^{\beta\omega} - 1}, \quad (\text{C2})$$

where Eq. (A7) is used. The average $\langle \cdots \rangle_0$ in Eq. (C2) is over the bath Hamiltonian in Eq. (24) as described in Appendix B. The integral in Eq. (C2) is evaluated by a 68-point Laguerre quadrature.

APPENDIX D: DECAY TIME

To obtain the relation in Eq. (47) of the text in the context of MTGLE, we make use of notation and formal relationships previously set for MTGLE.^{10,16} We note that $C(t) = \dot{\chi}(t)$. We begin with the Laplace transform $\hat{\chi}(z)$ and the relation

$$\hat{\chi}(z) = [z^2 + \Omega_0^2 + z\hat{\beta}_1(z)]^{-1}, \quad (\text{D1})$$

where $\hat{\beta}_1(z)$ is the Laplace transform of the friction kernel and Ω_0 is the adiabatic frequency given by

$$\frac{1}{\Omega_0^2} = \int_0^\infty d\omega \frac{\rho(\omega)}{\omega^2}. \quad (\text{D2})$$

In the incoherent regime $\Omega_0 = 0$ [equivalent to $\rho(0)$ having a nonzero value] and

$$z\hat{\chi}(z) = [z + \hat{\beta}_1(z)]^{-1}. \quad (\text{D3})$$

Thus,

$$\lim_{z \rightarrow 0} [z + \hat{\beta}_1(z)] = \hat{\beta}_1(0) = \frac{1}{\lim_{z \rightarrow 0} z\hat{\chi}(z)}. \quad (\text{D4})$$

We have shown previously that¹⁶

$$\rho(\omega) = \frac{2}{\pi} \text{Re}[i\omega\hat{\chi}(i\omega)] \quad (\text{D5})$$

and thus

$$\frac{\pi}{2} \rho(0) = \lim_{\omega \rightarrow 0} \text{Re}[i\omega\hat{\chi}(i\omega)] = \lim_{z \rightarrow 0} z\hat{\chi}(z). \quad (\text{D6})$$

Combining Eqs. (D4) and (D6) yields

$$\frac{\pi}{2} \rho(0) = \frac{1}{\hat{\beta}_1(0)}. \quad (\text{D7})$$

From Eq. (D3) with $\chi(0)=0$, we have following Laplace inversion that

$$\dot{\chi}(t) = C(t) = \frac{1}{2\pi i} \int_{\gamma-i\infty}^{\gamma+i\infty} dz \frac{e^{zt}}{z + \hat{\beta}_1(z)}. \quad (\text{D8})$$

Assuming at large t that the integrand goes as

$$\frac{e^{zt}}{z + \hat{\beta}_1(0)}$$

due to rapid oscillation of the exponential part, we have

$$C(t) \cong e^{-\hat{\beta}_1(0)t} \quad (\text{D9})$$

and the decay time τ is given by

$$\tau = \frac{1}{\hat{\beta}_1(0)} = \frac{\pi}{2} \rho(0) \quad (\text{D10})$$

where Eq. (D7) is used. The relationship of τ to the integral over $C(t)$ in Eq. (47) is found from Eq. (2) with $\omega=0$.

- ¹N. Makri and D. E. Makarov, J. Chem. Phys. **102**, 4600 (1995).
- ²J. Cao, L. W. Ungar, and G. A. Voth, J. Chem. Phys. **104**, 4189 (1996).
- ³R. P. Feynman, Rev. Mod. Phys. **20**, 367 (1948).
- ⁴R. P. Feynman and A. R. Hibbs, *Quantum Mechanics and Path Integrals* (McGraw-Hill, New York, 1965).
- ⁵L. S. Schulmann, *Techniques and Applications of Path Integrals* (Wiley, New York, 1981).
- ⁶S. Kremp, M. Winterstetter, and W. Domcke, J. Chem. Phys. **102**, 6499 (1995).
- ⁷H. Mori, Prog. Theor. Phys. **33**, 423 (1965).
- ⁸R. Kubo, J. Phys. Soc. Jpn. **29**, 255 (1966).
- ⁹S. A. Adelman and J. D. Doll, J. Chem. Phys. **61**, 4242 (1974); **64**, 2375 (1976).
- ¹⁰S. A. Adelman, Adv. Chem. Phys. **44**, 1431 (1980).
- ¹¹H. K. McDowell, J. Chem. Phys. **85**, 6034 (1986).
- ¹²H. K. McDowell, J. Chem. Phys. **86**, 1497 (1987).
- ¹³H. K. McDowell, Nucl. Phys. B **5**, 247 (1988).
- ¹⁴H. K. McDowell, Chem. Phys. **132**, 59 (1989).
- ¹⁵H. K. McDowell, J. Chem. Phys. **93**, 6723 (1990).
- ¹⁶A. M. Clogston and H. K. McDowell, Phys. Rev. B **44**, 4978 (1991).
- ¹⁷H. K. McDowell and A. M. Clogston, Phys. Rev. B **46**, 126 (1992).
- ¹⁸H. K. McDowell and A. M. Clogston, J. Stat. Phys. **67**, 331 (1992).
- ¹⁹H. K. McDowell, P. Tsai, and A. M. Clogston, Chem. Phys. Lett. **210**, 274 (1993).
- ²⁰H. K. McDowell and A. M. Clogston, J. Chem. Phys. **102**, 9026 (1995).
- ²¹H. K. McDowell and A. M. Clogston, Chem. Phys. **211**, 91 (1996).
- ²²A. M. Clogston and H. K. McDowell, Chem. Phys. (submitted).
- ²³H. K. McDowell and A. M. Clogston, J. Chem. Phys. **109**, 8249 (1998), preceding paper.
- ²⁴H. B. Shore and L. M. Sander, Phys. Rev. B **7**, 4537 (1973).
- ²⁵S. Rackovsky and R. Silbey, Mol. Phys. **25**, 61 (1973).
- ²⁶B. De Raedt and H. De Raedt, Phys. Rev. Lett. **50**, 1926 (1983).
- ²⁷S. Chakravarty and A. J. Leggett, Phys. Rev. Lett. **52**, 5 (1984).
- ²⁸B. De Raedt and H. De Raedt, Phys. Rev. B **29**, 5325 (1984).
- ²⁹A. Garg, Phys. Rev. B **32**, 4746 (1985).
- ³⁰B. Carmelli and D. Chandler, J. Chem. Phys. **82**, 3400 (1985); **89**, 452 (1988).
- ³¹A. Garg, J. N. Onuchic, and V. Ambegaokar, J. Chem. Phys. **83**, 4491 (1985).
- ³²A. J. Leggett, S. Chakravarty, A. T. Dorsey, M. P. A. Fisher, A. Garg, and W. Zwerger, Rev. Mod. Phys. **59**, 1 (1987).
- ³³H. K. McDowell, Chem. Phys. Res. **1**, 137 (1990).
- ³⁴R. D. Coalson, J. Chem. Phys. **86**, 995 (1987); **94**, 1108 (1991).
- ³⁵C. H. Mak and D. Chandler, Phys. Rev. A **41**, 5709 (1990); **44**, 2352 (1991).
- ³⁶J. S. Bader, R. A. Kuharski, and D. Chandler, J. Chem. Phys. **93**, 230 (1990).
- ³⁷A. Amann, J. Chem. Phys. **96**, 1317 (1992).
- ³⁸D. Vitali, L. Bonci, R. Mannella, and P. Grigolini, Phys. Rev. A **45**, 2285 (1992).
- ³⁹C. H. Mak, Phys. Rev. Lett. **68**, 899 (1992).
- ⁴⁰J. N. Gehlen and D. Chandler, J. Chem. Phys. **97**, 4958 (1992).

- ⁴¹J. N. Gehlen, D. Chandler, H. J. Kim, and J. T. Hynes, *J. Phys. Chem.* **96**, 1748 (1992).
- ⁴²C. H. Mak and J. N. Gehlen, *Chem. Phys. Lett.* **206**, 130 (1993).
- ⁴³J. Tang, *J. Chem. Phys.* **98**, 6263 (1993); **99**, 5828 (1993); *Chem. Phys. Lett.* **217**, 55 (1994).
- ⁴⁴X. Song and R. A. Marcus, *J. Chem. Phys.* **99**, 7768 (1993).
- ⁴⁵X. Song and A. A. Stuchebrukhov, *J. Chem. Phys.* **99**, 969 (1993).
- ⁴⁶D. Xu and K. Schulten, *Chem. Phys.* **182**, 91 (1994).
- ⁴⁷D. Kostic, Z. Ivic, D. Kapor, and A. Tancic, *J. Phys.: Condens. Matter* **6**, 729 (1994).
- ⁴⁸D. Vitali, P. Allegrini, and P. Grigolini, *Chem. Phys.* **180**, 297 (1994).
- ⁴⁹R. Egger, C. H. Mak, and U. Weiss, *J. Chem. Phys.* **100**, 2651 (1994).
- ⁵⁰C. H. Mak and R. Egger, *Phys. Rev. E* **49**, 1997 (1994).
- ⁵¹Y. Dakhnovskii, *J. Chem. Phys.* **100**, 6492 (1994).
- ⁵²R. D. Coalson, D. G. Evans, and A. Nitzan, *J. Chem. Phys.* **101**, 436 (1994).
- ⁵³D. G. Evans and R. D. Coalson, *J. Chem. Phys.* **102**, 5658 (1995).
- ⁵⁴M. Winterstetter and W. Domcke, *Chem. Phys. Lett.* **236**, 445 (1995).
- ⁵⁵G. Stock, *J. Chem. Phys.* **103**, 1561 (1995).
- ⁵⁶J. T. Stockburger and C. H. Mak, *J. Chem. Phys.* **105**, 8126 (1996).
- ⁵⁷D. R. Reichman, F. L. H. Brown, and P. Neu, *Phys. Rev. E* **55**, 2328 (1997).
- ⁵⁸T. P. Pareek, M. C. Mahato, and A. M. Jayannavar, *Phys. Rev. B* **55**, 9348 (1997).
- ⁵⁹R. Egger, H. Grabert, and U. Weiss, *Phys. Rev. E* **55**, R3809 (1997).
- ⁶⁰U. Weiss, *Quantum Dissipative Systems* (World Scientific, Singapore, 1993).
- ⁶¹J. T. Stockburger and C. H. Mak, *Phys. Rev. Lett.* **80**, 2657 (1998).
- ⁶²I. Turek, *J. Phys. C* **21**, 3251 (1988).
- ⁶³L. Hagg and O. Goscinski, *J. Phys. B* **26**, 2345 (1993).
- ⁶⁴M. Abramowitz and I. A. Segun, *Handbook of Mathematical Functions* (Dover, New York), Sec. 25.4.
- ⁶⁵R. G. Gordon, *Adv. Magn. Reson.* **3**, 1 (1968).
- ⁶⁶R. G. Gordon, *Adv. Chem. Phys.* **15**, 79 (1969).
- ⁶⁷B. J. Berne and G. D. Harp, *Adv. Chem. Phys.* **17**, 63 (1970).
- ⁶⁸S. F. Gull and G. J. Daniell, *Nature (London)* **272**, 686 (1978).
- ⁶⁹X. Zhuang, R. M. Haralick, and Y. Zhao, *IEEE Trans. Signal Process.* **39**, 1478 (1991).
- ⁷⁰A. Wragg and D. C. Dowson, *IEEE Trans. Inf. Theory* **IT-16**, 226 (1970).
- ⁷¹B. R. Frieden, *J. Opt. Soc. Am.* **62**, 511 (1972).
- ⁷²Y. Alhassid, N. Agmon, and R. D. Levine, *Chem. Phys. Lett.* **53**, 22 (1978).
- ⁷³M. R. Teague, *J. Opt. Soc. Am.* **70**, 920 (1980).
- ⁷⁴R. D. Levine, *J. Phys. A* **13**, 91 (1980).
- ⁷⁵R. D. Levine, *Adv. Chem. Phys.* **47**, 239 (1981).
- ⁷⁶L. R. Mead and N. Papanicolaou, *J. Math. Phys.* **25**, 2404 (1984).
- ⁷⁷N. S. Tzannes and P. A. Jonnard, *Opt. Eng. (Bellingham)* **26**, 1077 (1987).
- ⁷⁸A. Tagliani, *J. Math. Phys.* **34**, 326 (1993).
- ⁷⁹E. T. Jaynes, *Proc. IEEE* **70**, 939 (1982).
- ⁸⁰B. R. Frieden, *Proc. IEEE* **73**, 1764 (1985).
- ⁸¹J. E. Shore and R. W. Johnston, *IEEE Trans. Inf. Theory* **IT-26**, 26 (1980).
- ⁸²R. W. Harrison, *Acta Crystallogr. A* **45**, 4 (1989).
- ⁸³R. N. Silver, D. S. Sivia, and J. E. Gubernatis, *Phys. Rev. B* **41**, 2380 (1990).
- ⁸⁴J. E. Gubernatis, M. Jarrell, R. N. Silver, and D. S. Sivia, *Phys. Rev. B* **44**, 6011 (1991).
- ⁸⁵E. Gallicchio and B. J. Berne, *J. Chem. Phys.* **101**, 9909 (1994).